

# Ultrafast pulse-amplitude modulation with a femtojoule silicon photonic modulator

RAPHAËL DUBÉ-DEMERS, SOPHIE LAROCHELLE, AND WEI SHI\*

Department of Electrical and Computer Engineering, Centre d'Optique, Photonique et Laser (COPL), Université Laval, Québec, Québec, Canada

\*Corresponding author: wei.shi@gel.ulaval.ca

Received 14 January 2016; revised 8 April 2016; accepted 4 May 2016 (Doc. ID 257360); published 9 June 2016

Ultrahigh-speed optical interconnects are essential to future cloud computing. Further increase in optical transmission speed has been hindered by power consumption and limited bandwidth resources, for which integrated optical transceivers using advanced modulation formats, such as pulse-amplitude modulation (PAM), are a promising solution. We report 80 Gb/s PAM operation of a silicon microring modulator (MRM) with an ultralow power consumption below 7 fJ/bit. We also report the first demonstration of PAM-8 modulation of MRMs in the Gb/s order, achieving error-free capability at 45 Gb/s, using 1 fJ/bit. To the best of our knowledge, these results feature the lowest power consumption, per transmitted bit, ever demonstrated at such high data rates. We further demonstrate PAM data transmission up to 64 Gb/s over 5 km. Simultaneous achievement of ultrafast modulation and ultralow power consumption is a critical step toward next-generation optical interconnects. © 2016 Optical Society of America

**OCIS codes:** (130.4110) Modulators; (060.4510) Optical communications; (130.0130) Integrated optics; (230.5750) Resonators.

<http://dx.doi.org/10.1364/OPTICA.3.000622>

## 1. INTRODUCTION

Transition to next-generation optical interconnects is driven by the demand for ultrahigh-speed data transmission in computing systems [1] and data centers for the cloud [2]. Key enablers of this transition have been identified as further advances in photonic integration and high-speed, low-power complementary metal-oxide semiconductor (CMOS) circuits. Leveraging well-developed CMOS fabrication processes, silicon photonics has quickly emerged as the preferred technology for large-scale photonic integration. In particular, silicon microring modulators (MRMs) are among the most promising solutions for integrated optical transmitters since they combine many desirable features, such as low power consumption, compactness, and CMOS compatibility [3]. Using a MRM, 60 Gb/s on-off keying (OOK) transmission has been demonstrated [4]. Ultralow power of 1 fJ/bit was also reported, but running at a relatively low data rate of 25 Gb/s [5]. An eight-channel wavelength division multiplexing (WDM) transmitter based on MRMs, each channel operating at 40 Gb/s at 32 fJ/bit, was recently reported [6]. Finally, a novel approach using a Bragg grating as the optical cavity, demonstrates 60 Gb/s operation [7].

Future interconnects desire a higher data rate per wavelength to minimize the number of WDM channels. However, the path toward higher speed has been hindered by the power consumption and limited bandwidth of electronic circuits, not to mention the difficulty of integrating laser sources on silicon. First, MRMs suffer from the intrinsic trade-off between modulation efficiency and bandwidth [5,8,9] because the photon lifetime limits how fast the optical cavity can be modulated. Consequently, high-speed

MRMs are usually designed with a low quality factor ( $Q$ ) for a wide bandwidth, thereby sacrificing modulation efficiency. In addition, the power consumption of driving and logic circuits scales up quickly with the frequency. High-speed, low-power drivers are very challenging above 40 GHz.

Advanced modulation formats, such as pulse-amplitude modulation and quadrature phase-shift keying (QPSK), provide higher spectral efficiency, i.e., higher bit rates, within a given bandwidth [2]. Very limited experimental results have been reported for high-speed MRMs with high-order modulation formats, including 56 Gb/s [10] QPSK and 24 Gb/s PAM-4 [11]. Nevertheless, these devices have relatively high power consumptions in the range of a few tens to hundreds of fJ/bit. In addition, in the case of QPSK, coherent detection introduces extra complexity and cost. Therefore, direct detection is preferred for low-power optical interconnects. Although highly desired, simultaneous achievement of an ultrahigh-speed data rate beyond 40 Gb/s and ultralow power operation approaching one femtojoule per bit has not been demonstrated.

In this paper, we examine higher-order modulation of an optimized silicon MRM with the direct detection scheme for ultrahigh-speed optical interconnects. We present PAM operation of the MRM up to 80 Gb/s with an ultralow power consumption at the level of fJ/bit. We show significantly enhanced spectral efficiency of 2 and 3 bits per symbol with error-free capability. Transmission of a PAM-4 signal over 5 km of standard single-mode fiber (SSMF) at 64 Gb/s is also demonstrated. Our results further demonstrate the possibility to adapt the design to comply with commercial foundry rules, such as multiproject wafer (MPW) services.

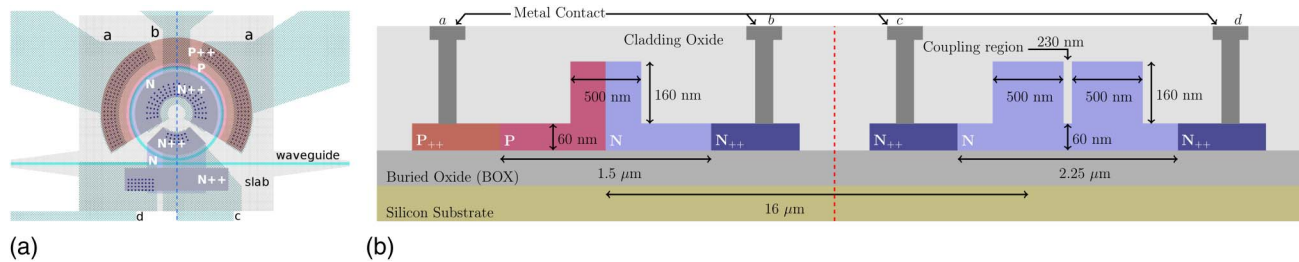


**Fig. 1.** (a) Partial layout of the mask used for the fabrication of the device. The resistive heater is present in the coupling region (bottom section). The slab is shown in gray, vias are shown as circles, and metal connections are shown in teal. The  $P$  and  $N$  dopant levels are used to implement the lateral p-n junction whereas the highly doped regions, i.e.,  $P_{++}$  and  $N_{++}$ , are used as ohmic contacts. The blue dashed line indicates the position of the cross section presented in (b). (b) Vertical and centered cross section of the modulator, from top to bottom in (a) (not to scale). The red dashed line represents the center of the ring. The left-hand side represents the p-n junction of the modulator with metal contacts  $a$  and  $b$  used to transmit the signal. The right-hand side represents the coupling region and the heater. The heater is controlled via metal contacts  $c$  and  $d$ . From the graphical representation, it is obvious that the ring and bus waveguides are heated together, thus minimizing the impact on the coupling conditions.

This paper is organized as follows. Section 2 provides information on design and fabrication, followed by the characterization of the modulator under direct current (DC) and small-signal operation. Based on the measured results, the extinction ratio (ER) and electro-optic (EO) bandwidth are extracted from the measurements and the inherent trade-off discussed. Specifically, it is shown that **the optimal operating point depends on the targeted operating speed**. Section 3 presents our experimental results and bit error rate (BER) measurements regarding PAM modulation and transmission. Section 4 provides information on the evaluation of the power consumption of the modulator.

## 2. DEVICE DESIGN AND CHARACTERIZATION

We designed and optimized the modulator with the aid of the **dynamical model presented** in [8]. As illustrated in Fig. 1, it makes use of the plasma dispersion effect through carrier depletion in a lateral p-n junction on a **220 nm** thick silicon-on-insulator (SOI) wafer. A 60-nm-thick slab is used for electrical connections. The MRM has a radius of **8 μm** and a coupling gap of 230 nm. The heavily doped regions for metal contacts are 500 nm away from the edge of the 220-nm-high, 500-nm-wide rib waveguide. These parameters were chosen to achieve the critical coupling condition and maximize dynamic extinction ratio, following the methodology given in [8]. Due to fabrication process variations, we observed a variation of up to 10 dB in the DC

ER, i.e., from 25 to 35 dB of ER. However, we obtained similar performance, even with SOI chips having lower ER. This is in part because we operate the MRM at high frequency detuning. In this case, **the optical modulation amplitude (OMA) is not significantly sensitive to variations of the DC ER**.

A semiconductor heater is included in the design for wavelength tuning, to compensate for fabrication errors and temperature fluctuations. The p-n junction for intracavity modulation spans roughly 70% of the circumference, and the heater spans roughly 20% of the circumference. On-chip optical input/output (I/O) is achieved via surface grating couplers for TE-polarized light. The modulator was fabricated through the MPW service at IMEC, Belgium.

The measured static responses at various applied voltages are presented in Fig. 2(a). We measure a very high resonance depth of 35 dB at zero bias, indicating that the modulator is in the critical coupling condition, i.e., the round-trip propagation loss of light in the ring cavity is equal to the loss due to the coupling to the bus waveguide. **Sufficient ER is important for achieving high-order PAM modulation**. Figure 2(a) also provides further indication of the presence of the critical coupling condition. It shows that the resonance depth decreases as the forward potential increases, indicating an undercoupling condition in forward bias due to the **increased free carriers in the waveguide and thus increased absorption loss**. The figure also shows that the resonance depth decreases as the reverse potential increases, indicating an overcoupling condition in reverse bias. The resonance shift as a function of

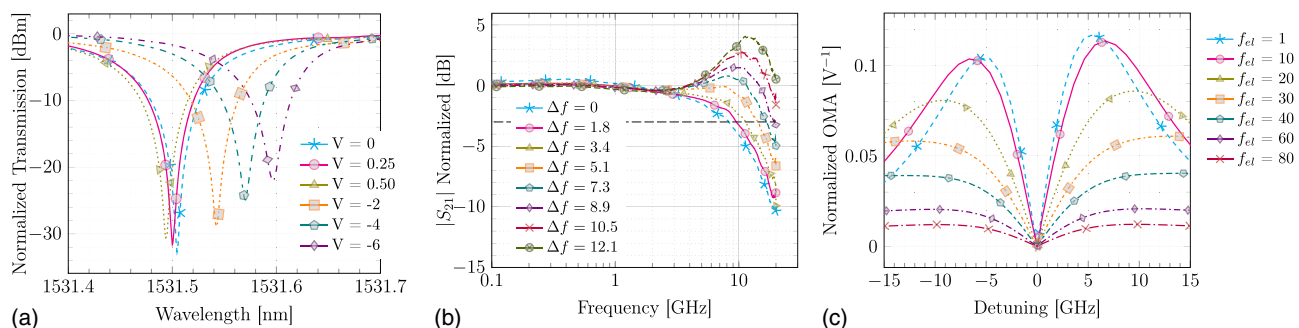


**Fig. 2.** (a) Measured power transmission spectra in the vicinity of a resonance. The DC voltages are noted in units of volt. (b) Measured EO scattering parameter  $S_{21}$  as a function of the frequency.  $S_{21}$  values are measured for various detuning frequencies, here noted in gigahertz, and normalized at 100 MHz. The dashed horizontal line indicates the -3 dB level. (c) Predicted OMA as a function of the optical detuning. The driving modulation frequency  $f_{el}$  is indicated in gigahertz and the predictions are done with the aid of the dynamical model [8].

voltage shows an efficiency of about 2 GHz/V, which is among the highest values reported for a lateral p–n junction in the depletion mode. Also, the measured free spectral range (FSR) is 12.14 nm and the quality factor is 18,000, at equilibrium.

### A. Bandwidth–Efficiency Trade-Off

The frequency responses of the MRM are measured and shown in Fig. 2(b). The bandwidth is measured through the  $S_{21}$  scattering parameter, as a function of the frequency. Measurements are done with varied frequency detuning  $\Delta f$ , here defined as the frequency  $f_{\text{op}}$  of the optical input minus the resonant frequency  $f_{\text{res}}$  of the cavity, i.e.,  $\Delta f = f_{\text{op}} - f_{\text{res}}$ . Figure 2(b) clearly shows the presence of the modulation resonance [12]. This representation is useful to extract bandwidth information at a given detuning state. However, the choice of the optimal operating point is a result of the trade-off between the modulation bandwidth and modulation depth. On one hand, it is generally accepted that the EO bandwidth is proportional to the optical detuning, as per Fig. 2(b). On the other hand, the DC representation of the OMA is often used and allows one to conclude that, for an infinitesimal small-signal excitation, the OMA is proportional to the detuning up to a given point where the relation becomes inversely proportional, substantiating the so-called bandwidth–efficiency trade-off. In addition, we here corroborate the fact that this particular trade-off is also a function of the operating speed and that it cannot be specified only in terms of optical detuning, as noted by Yu *et al.* [9]. The relation between the OMA and bandwidth as a function of the frequency detuning is expressed, for our modulator, in Fig. 2(c), where the normalized OMA is here defined as the difference between the maximum  $P_{\text{max}}$  and minimum  $P_{\text{min}}$  optical power when driven by a small signal over the voltage amplitude  $V_{p-p}$  times the input optical power  $P_{\text{in}}$ , i.e.,  $1 (P_{\text{max}} - P_{\text{min}}) / (V_{p-p} \cdot P_{\text{in}})$ . For instance, in our case, the optimal operating point at 10 GBaud would be  $\Delta f \sim 7$  GHz, whereas it would be  $\Delta f \sim 11$  GHz at 40 GBaud.

For the BER measurements of the forthcoming section, we operate the device at a detuning of roughly 10 GHz. Since the vector network analyzer used is limited at 20 GHz, we extrapolate the  $S_{21}$  curve with the aid of the dynamical model [8], and find the –3 dB bandwidth to be 25 GHz at a detuning of 10 GHz. Since we consider a non-return-to-zero modulation scheme, the spectrum of the signal is thus proportional to a  $\text{sinc}^2$  of the modulation speed. Such signal has most of its power inside spectral components with frequency below half of the operating frequency [13]. Additionally, due to the high frequency detuning used in the current demonstration, the insertion loss in the coming transmission experiment is consistently measured below 1 dB.

## 3. HIGH-SPEED MODULATION AND TRANSMISSION

A schematic of the test bench for large-signal modulation and transmission is shown in Fig. 3. We use a BER test system as a pseudo-random binary sequence (PRBS) of  $2^{15} - 1$  and clock source. The PRBSs are combined and regenerated with a 3 bit digital-to-analog converter (DAC). The output of the DAC needs to be carefully chosen to linearize the optical output of the PAM signals; see Supplement 1. We use two channels of the DAC for PAM-4 and three for PAM-8. The analog signal is then amplified with a 55 GHz radio-frequency (RF) amplifier and biased with a

70 GHz bias tee. The electrical signal is then sent via a 50 GHz RF, 50  $\Omega$  terminated, ground–signal–ground configured microprobe. We use a polarization maintaining fiber, fed with a tunable laser as the optical input, to ensure an optimal coupling with the surface grating couplers. A 250  $\mu\text{m}$  spaced fiber array is used to input and collect the light to and from the SOI chip. The measured fiber-to-fiber insertion loss of the SOI chip is 12.8 dB. We use an optical isolator at the output of the chip followed by an erbium-doped fiber amplifier (EDFA) to amplify the modulated signal. The amplified spontaneous emission is filtered out by using an optical filter. Then, a tunable optical attenuator is used to control the received power. A 70 GHz photodetector is used to achieve optical-to-electrical conversion. The electrical signal is acquired with a 30 GHz analog bandwidth, 80 Gsamples/s real-time oscilloscope (RTO). Finally, off-line signal processing, including filtering, resampling, and BER counting, is performed numerically.

We examine the performance of the modulator by first considering the PAM eye diagrams collected by the RTO, as shown in Fig. 4, representing examples of the data captured for BER measurements. Figure 4(a) shows a 30 Gb/s OOK signal as observed at the RTO, whereas Fig. 4(b) shows a 80 Gb/s PAM-4 signal after equalization. In addition, one can observe the degradation due to the transmission over 5 km by visually comparing Figs. 4(c) and 4(d). It is also possible to observe the improvement due to the equalization by considering Figs. 4(e) and 4(f). For the purpose of demonstration, the signals have been upsampled to produce the eye-diagrams using an anti-aliasing finite-impulse response filter. Note that this filter is not applied on the signals that are used for BER computations. In addition to the electrical eye diagrams, optical eyes are provided in Supplement 1.

In the transmission experiment, the modulator is driven by peak-to-peak voltages ( $V_{p-p}$ ) of 3.5 V and 2.2 V for PAM-4 and PAM-8, respectively. The OOK case uses 4 V of  $V_{p-p}$ . The low voltage required to drive the PAM-8 cases demonstrates the possibility of integration between the silicon chip and the CMOS driver. Doing such an integration would be beneficial since it would dramatically reduce the cost and power consumption of the transmitter. The modulator is biased at –5.5 V and operated at  $\Delta f \sim 10$  GHz. It is also important to note that, with respect to our setup, we do not apply any kind of digital signal processing at the transmitter. The contributions from additional signal impairments, such as the power penalty due to the chirp, are investigated in Supplement 1. It is noteworthy that, under the aforementioned operating conditions, i.e.,  $\Delta f > 0$ , the chirp leads to pulse compression. Nonetheless, the power penalty

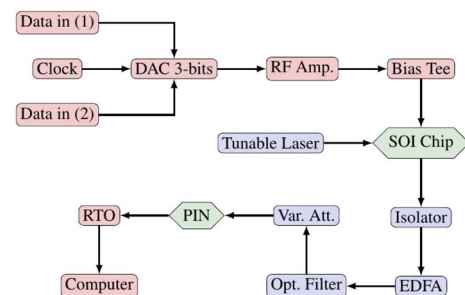


**Fig. 3.** Schematic of the test bench we use for BER measurements. In the transmission experiments, SSMFs of various lengths are introduced between the optical filter and variable attenuator (not shown in the schematic).



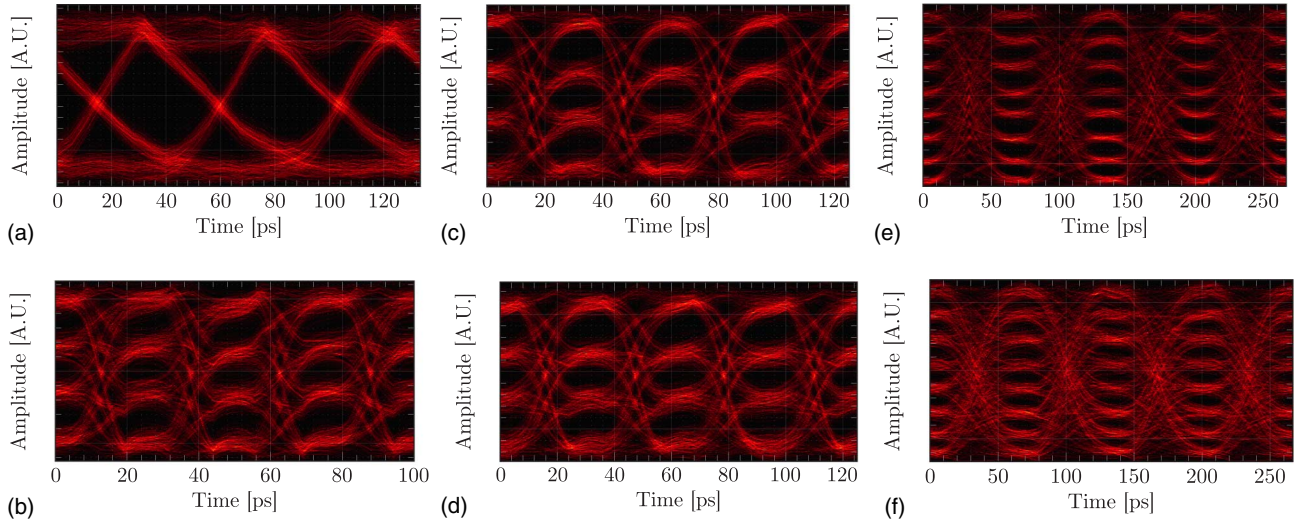


**Fig. 4.** Electrical eye diagrams collected at the RTO after optical-to-electrical conversion. (a) OOK at 30 Gb/s, 3.5 dBm of received power. (b) PAM-4 at 80 Gb/s, 7 dBm of received power, equalized. (c) and (d) PAM-4 at 64 Gb/s, 7 dBm of received power, equalized, for back-to-back and 5 km transmission, respectively. (e) and (f) PAM-8 at 45 Gb/s, 7 dBm of received power; the former is equalized.

induced by the chirp,  $\delta\nu$ , is not significant. For example, for a 40 Gb/s OOK signal, detuned at  $\Delta f = 10$  GHz, and driven by 4 V of  $V_{p-p}$ , the calculation results in a negative power penalty of  $-0.23$  dB, for a frequency chirp of 2.27 GHz, the maximum observed in the time-domain responses. Additional information on the modeling of the chirp is provided in Supplement 1, along with an estimation of the signal degradation due to nonlinear effects from the build-up of optical power inside the cavity.

At the receiver side, we acquire the data at 80 GSa/s and apply a super-Gaussian, fourth-order filter. The signal is then resampled to 1 sample per bit. The optimal sampling time is taken such that the probability density function (PDF) of each level is best resolved. At this point, the  $N - 1$  optimal decision thresholds are found, where  $N$  is the PAM order. Optimal decision thresholds are taken to be at the  $N - 1$  local minima formed by the total PDF of the PAM signal. This is valid under the assumption that the  $N$  PDFs are Gaussian and equivalent, i.e., each symbol is equiprobable. Measured PDFs taken at the optimal instant for the decision threshold, along with their Gaussian fits, are provided

in Supplement 1. A first round of BERs is computed, providing the raw, or unequalized, BERs.

The resampled data stream is then filtered with a minimum mean square error (MMSE) filter. To create the MMSE estimator, we use a known sequence of transmitted bits, i.e., a training of 2000 bits. A Toeplitz matrix  $X$  is populated by the discrete autocorrelation function of the received signal, computed up to a delay  $\tau_X$ . In this paper, our results have been computed with  $\tau_X = 50$ . An estimate  $R$  of  $X$  is computed,  $R = X^T X$ . At the same time, the cross-correlation  $Q$  between the received signal and known sequence is computed up to a delay  $\tau_Q = \tau_X/2$ . The coefficient of the estimator  $\mathcal{E}$  is then obtained in a straightforward manner, i.e.,  $\mathcal{E} = R \backslash Q$ . The equalized data are finally obtained by computing the convolution between the received data and  $\mathcal{E}$ . Hence, the MMSE equalization we employ uses fixed coefficients and is not adaptive. A second round of BERs is then computed, providing the equalized BERs.

Figure 5 shows the measured BERs in back-to-back and after 5 km SSMF transmission. Data before and after equalization are

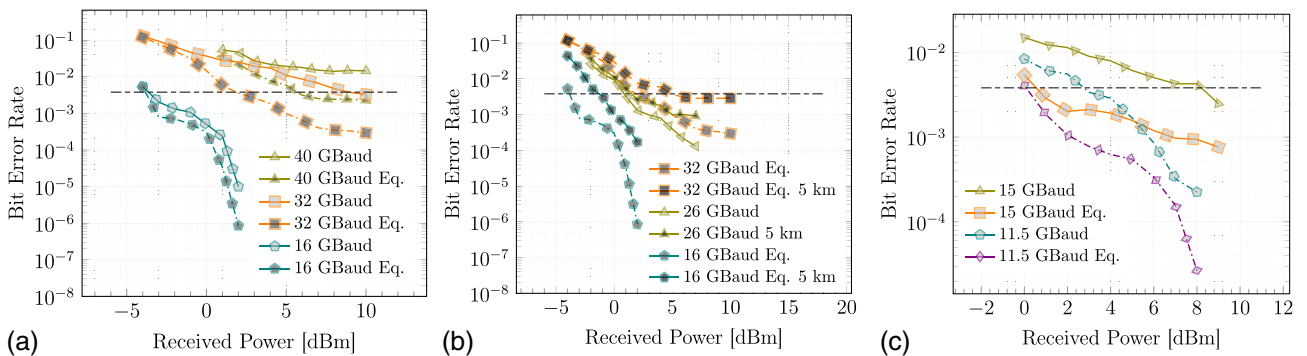


**Fig. 5.** Measured BERs. (a) PAM-4 in a back-to-back configuration; BER below the pre-FEC threshold is demonstrated up to 80 Gb/s using equalization and up to 64 Gb/s without equalization. (b) PAM-4 back-to-back and after 5 km of SSMF. BER below the pre-FEC threshold is demonstrated up to 64 Gb/s using equalization and up to 52 Gb/s without equalization. (c) PAM-8 back-to-back. Modulation of PAM-8 signal with a BER below the pre-FEC threshold is demonstrated up to 45 Gb/s without using equalization. The curves in (a) and (c) highlight the effect of the equalization, whereas the effect of the distance and associated power penalty is shown in (b). The dashed horizontal lines mark the pre-FEC threshold.

presented for PAM-4 up to 40 GBaud (80 Gb/s) and for PAM-8 up to 15 GBaud (45 Gb/s). We see that the transmission of a 40 GBaud PAM-4 signal at a reasonable BER is possible only when the equalization scheme is used. In contrast, PAM-4 at 32 GBaud and PAM-8 at 15 GBaud are possible even without using equalization. The seemingly high received power is because no RF amplifier has been used after the photodetector, and the sensitivity of our RTO is relatively low. Our setup is thus limited by a noise floor of  $-7$  dBm. The received powers for given BERs could be reduced by improving the noise floor of our setup.

Based on the OT4U standard [14], we consider that a 6.7% forward error correction (FEC) overhead can be used such that pre-FEC BER below  $3.8 \times 10^{-3}$  can be regarded as error-free, i.e., the post-FEC BER will be below  $10^{-15}$  [15,16]. This FEC threshold is denoted by a black dashed lines in Fig. 5(a)–5(c). In addition, we consider Gray coding when counting the BER, i.e., the BER is further reduced by a  $1/\log_2(N)$  factor, assuming that erroneous symbol decisions are made to the closest neighboring symbols. As shown in Fig. 5(b), data transmission over 5 km with a BER below the pre-FEC threshold has been achieved for PAM-4 up to 64 Gb/s with equalization and up to 52 Gb/s (26 GBaud) without equalization. We notice that the latter result is compliant with emerging IEEE802.3bs standards, specifically for 400 Gb/s Ethernet at 2 km, where the use of PAM-4 at 26.6 GBaud before FEC has been proposed [17].

#### 4. POWER CONSUMPTION

Electrical power is dissipated inside the modulator on rising transitions, charging the capacitor, of capacitance  $C$ , in the depletion region of the p-n junction. In this case, the energy  $E$  consumed by a rising transition of magnitude  $V$  is given by  $E = CV^2$  [18]. Since PAM modulation formats inherently contain multiple transitions occurring at different magnitudes, it is more convenient to find an expression for the total energy consumed  $E_T$  by all rising transitions as a function of  $V_{p-p}$ . Under the assumption that levels in a given PAM signal are equally distributed inside  $V_{p-p}$ ,  $E_T$  is given by

$$E_T = CV_{p-p}^2 \sum_{i=1}^{N-1} (N-i) \left( \frac{i}{N-1} \right)^2, \quad (1)$$

where, we recall,  $N$  is defined as the PAM order. There are  $N^2$  possible transitions in a PAM signal and  $\log_2(N)$  bit(s) per symbol, so the energy consumed per bit  $E_b$  is given by

$$E_b = \frac{E_T}{N^2 \log_2(N)}. \quad (2)$$

To evaluate the power consumption of the modulator, we measured its small-signal frequency responses, and we extracted the capacitance  $C_{pn}$  of the p-n junction under equilibrium. The value of  $C_{pn}$  under operating conditions, i.e.,  $-5.5$  V of applied bias, is computed at  $C_{pn} = 9.4$  fF using the model presented in [8]. Therefore, the estimated effective power consumption, i.e., the power that goes through the p-n junction and acts as the modulating force, is 6.5 fJ/bit at 40 GBaud, PAM-4, and is 1 fJ/bit for PAM-8 at 15 GBaud. Under operating conditions, the electrical bandwidth is evaluated at 32 GHz. A thorough description of the measurement of  $C_{pn}$ , as well as further estimations of the power consumption, are provided in Supplement 1.

We measured the efficiency of the heater to be 33  $\mu\text{W}/\text{GHz}$ . However, the heater has been included as a proof of concept rather than as an optimized heater. Nevertheless, this value is comparable to previous demonstrations [19,20], but at much higher modulation speeds. For instance, 130 fJ/bit would be necessary to compensate for a  $10^\circ\text{C}$  at 80 Gb/s. Details and suggestions to improve the efficiency are discussed in Supplement 1. An improved efficiency could help to bring down the power consumption of the heater to 5 fJ/bit [21].

#### 5. CONCLUSION

We have demonstrated ultrahigh-speed, ultralow-power PAM operation with a silicon photonic modulator. Direct detection below the pre-FEC threshold has been achieved up to 80 and 45 Gb/s for PAM-4 and PAM-8, respectively. The power consumed by optical modulation has been estimated to be as low as 1 fJ/bit and 6.5 fJ/bit for PAM-8 and PAM-4, respectively. To the best of our knowledge, both values are the lowest yet demonstrated at such high data rates. In addition, data transmission over 5 km has been demonstrated for PAM-4 up to 64 Gb/s with equalization and up to 52 Gb/s (26 GBaud) without equalization. It is shown that higher-order modulation formats can significantly increase the data rate given the efficiency–bandwidth trade-off of a resonator modulator; in the present work, this is 2 and 3 bits per symbol for PAM-4 and PAM-8, respectively. The enhanced spectral efficiency may drastically reduce the required operating frequency and power consumption of driving and logic circuits for a CMOS-photonic integrated system. These results and findings reveal that silicon resonator modulators with advanced modulation formats are capable of delivering ultrahigh data rates (toward 100 Gb/s per channel) with ultralow power consumption at the level of fJ/bit, indicating a promising path toward future ultrafast optical interconnects.

**Funding.** Natural Sciences and Engineering Research Council of Canada (NSERC) (RDCPJ438811-12); PROMPT (PJT-2011-17); Fonds de Recherche du Québec-Nature et Technologies (FRQNT) (2016-NC-190737).

**Acknowledgment.** The authors thank K. Bédard and P. Chrétien from COPL for technical support. We further thank CMC Microsystems for enabling the chip fabrication at IMEC, Belgium. We are thankful to M. Caillet from Rohde & Schwartz for fruitful discussion on  $S$  parameter measurements. We finally acknowledge the Large Time/Frequency Analysis Toolbox (LTFAT) group for their reassignment method [22].

See Supplement 1 for supporting content.

#### REFERENCES

1. G. Li, A. V. Krishnamoorthy, I. Shubin, J. Yao, Y. Luo, H. Thacker, X. Zheng, K. Raj, and J. E. Cunningham, "Ring resonator modulators in silicon for interchip photonic links," *IEEE J. Sel. Top. Quantum Electron.* **19**, 3401819 (2013).
2. Y. Kai, M. Nishihara, T. Tanaka, and T. Drenski, "Experimental comparison of pulse amplitude modulation PAM and discrete multi-tone DMT for short-reach 400-Gb/s data communication," in *European Conference on Optical Communications (ECOC)* (2013), paper Th1F3.
3. W. Bogaerts, P. De Heyn, T. Van Vaerenbergh, K. De Vos, S. K. Selvaraja, T. Claes, P. Dumon, P. Bienstman, D. Van Thourhout, and

- R. Baets, "Silicon microring resonators," *Laser Photon. Rev.* **6**, 47–73 (2012).
4. X. Xiao, H. Xu, X. Li, Z. Li, T. Chu, J. Yu, and Y. Yu, "60-Gb/s silicon modulators with enhanced electro-optical efficiency," in *Optical Fiber Communication Conference (OFC)* (2013), paper OW4J.3.
5. E. Timurdogan, C. M. Sorace-Agaskar, J. Sun, E. S. Hosseini, A. Biberman, and M. R. Watts, "An ultralow power athermal silicon modulator," *Nat. Commun.* **5**, 4008 (2014).
6. Y. Liu, R. Ding, Q. Li, Z. Xuan, Y. Li, Y. Yang, A. E. Jim, P. G. Q. Lo, K. Bergman, T. Baehr-Jones, and M. Hochberg, "Ultra-compact 320-Gb/s and 160-Gb/s WDM transmitters based on silicon microrings," in *Optical Fiber Communication Conference (OFC)* (2014), paper Th4G.6.
7. K. Bédard, A. D. Simard, B. Fillion, Y. Painchaud, L. A. Rusch, and S. LaRochelle, "Dual phase-shift Bragg grating silicon photonic modulator operating up to 60 Gb/s," *Opt. Express* **24**, 2413–2419 (2016).
8. R. Dubé-Demers, J. St-Yves, A. Bois, Q. Zhong, M. Caverley, Y. Wang, L. Chrostowski, S. LaRochelle, D. V. Plant, and W. Shi, "Analytical modeling of silicon microring and microdisk modulators with electrical and optical dynamics," *J. Lightwave Technol.* **33**, 4240–4252 (2015).
9. H. Yu, D. Ying, M. Pantouvaki, J. Van Campenhout, P. Absil, Y. Hao, J. Yang, and X. Jiang, "Trade-off between optical modulation amplitude and modulation bandwidth of silicon micro-ring modulators," *Opt. Express* **22**, 15178–15189 (2014).
10. P. Dong, C. Xie, L. L. Buhl, and Y. K. Chen, "Silicon microring modulators for advanced modulation formats," in *Optical Fiber Communication Conference (OFC)* (2013), paper OW4J.2.
11. L. Wang, R. Hu, L. M. Feng, Y. Qiu, X. Xiao, D. Chen, Q. Yang, S. Yu, Z. Li, J. Yu, and Y. Yu, "Transmission of 24-Gb/s PAM-4 over 150-km SSMF using a driverless silicon microring modulator," in *Asia Communications and Photonics Conference (ACPC)* (2014), paper ATh4D.
12. W. D. Sacher and J. K. S. Poon, "Dynamics of microring resonator modulators," *Opt. Express* **16**, 15741–15753 (2008).
13. M. C. Gupta and J. Ballato, *The Handbook of Photonics* (CRC Press, 2007).
14. "Media access control parameters, physical layers, and management parameters for 40-Gb/s and 100-Gb/s operation," IEEE Std. 802.3ba (2010).
15. J. Cho, C. Xie, and P. J. Winzer, "Analysis of soft-decision FEC on non-AWGN channels," *Opt. Express* **20**, 7915–7928 (2012).
16. "Forward error correction for high bit-rate DWDM submarine systems," ITU-T Recommendation G.975.1 (2004).
17. "IEEE P802.3bs 400-Gb/s Ethernet Task Force," IEEE Std. 802.3bs (2015).
18. M. R. Watts, W. A. Zortman, D. C. Trotter, R. W. Young, and A. L. Lentine, "Vertical junction silicon microdisk modulators and switches," *Opt. Express* **19**, 21989–22003 (2011).
19. W. A. Zortman, A. L. Lentine, D. C. Trotter, and M. R. Watts, "Integrated CMOS compatible low power 10-Gb/s silicon photonic heater-modulator," in *Optical Fiber Communication Conference (OFC)* (2012), paper OW4I.5.
20. G. Li, X. Zheng, J. Yao, H. Thacker, I. Shubin, Y. Luo, K. Raj, J. E. Cunningham, and A. V. Krishnamoorthy, "25-Gb/s 1-V driving CMOS ring modulator with integrated thermal tuning," *Opt. Express* **19**, 20435–20443 (2011).
21. Z. Lu, K. Murray, H. Jayatilaka, and L. Chrostowski, "Michelson interferometer thermo-optic switch on SOI with a 50- $\mu$ W power consumption," *IEEE Photon. Technol. Lett.* **27**, 2319–2322 (2015).
22. Z. Průša, P. L. Søndergaard, N. Holighaus, C. Wiesmeyer, and P. Balazs, "The large time-frequency analysis toolbox 2.0," in *Sound, Music, and Motion*, M. Aramaki, O. Derrien, R. Kronland-Martinet, and S. Ystad, eds., *Lecture Notes in Computer Science* (Springer, 2014), pp. 419–442.